Chemical Geology 709 (2026) 123362

Contents lists available at ScienceDirect

Chemical Geology

journal homepage: www.elsevier.com/locate/chemgeo

Volatile evolution of silicic magmatic systems in the Central Main Ethiopian Rift: Insights from melt inclusions and apatite crystals of Tullu Moye and Boset volcanoes

Amdemichael Zafu Tadesse [a,b,c,*], V.C. Smith [d], K. Fontijn [e], J.C.M. De Hoog [f], D.J. Colby [g], M.C.S. Humphreys [g], T.A. Mather [a], D.M. Pyle [a]

[a] Department of Earth Sciences, University of Oxford, UK
[b] School of Earth Sciences, Addis Ababa University, Ethiopia
[c] Lamont-Doherty Earth Observatory, Columbia University, Palisades, USA
[d] School of Archaeology, University of Oxford, UK
[e] Department of Geosciences, Environment and Society, Université Libre de Bruxelles, Belgium
[f] Grant Institute, School of Geosciences, University of Edinburgh, UK
[g] Department of Earth Sciences, Durham University, UK

ARTICLE INFO

Editor: Dr. Claudia Romano

Keywords:
Apatite
Melt inclusions
Volatiles
Peralkaline magma
Main Ethiopian Rift

ABSTRACT

Magmatic volatile elements play a critical role in magma reservoir and ascent processes, from influencing the liquid line of descent to controlling magma storage dynamics and eruption style. However, constraining volatile behaviour prior to eruption remains challenging. This study presents a detailed model of pre-eruptive volatile content and evolution in a peralkaline magmatic system, based on integrated analyses of apatite crystals and glass (matrix and melt inclusions) from four explosive eruptions sourced from the Tullu Moye and Boset-Bericha volcanoes in the Main Ethiopian Rift. Apatite records from these eruptions indicate prolonged volatile-undersaturated conditions during magma crystallization at shallow crustal levels (~4–6 km depth). Thermodynamic modelling of measured apatite and melt inclusion compositions suggest that magmatic differentiation was the dominant control on volatile evolution during eruption. Apatite and melt inclusions from the Older Tullu Moye Pumice are compositionally distinct, exhibiting higher Cl and minor element contents (i.e., MgO) than those from subsequent comenditic eruptions at Tullu Moye and Boset-Bericha volcanoes. This likely reflects crystallization from a more primitive melt, associated with early-stage clinopyroxene phenocrysts of the Older Tullu Moye Pumice. Continued crystallization and differentiation in the Tullu Moye reservoir led to volatile and trace element enrichment, ultimately feeding the Younger Tullu Moye Pumice eruption. In contrast, the Boset-Bericha deposits show no comparable inter-eruption variation in magma composition, suggesting limited temporal evolution. Our integrated approach can be broadly applied to reconstruct the temporal evolution of pre-eruptive volatile behaviour in other volcanic systems.

1. Introduction

Magmatic volatiles (H_2O, S, CO_2, and halogens) are minor but important constituents of silicate melts at depth. Their compositions and concentrations influence mineral phase stability and the liquid line of descent (Zimmer et al., 2010), as well as key physical properties such as viscosity and melt density (Giordano et al., 2008; Lange and Carmichael, 1990). Upon volatile saturation, the exsolution of a fluid phase can drastically alter the bulk magma density, potentially causing pressure build-up within the magma storage region. Volatile exsolution and subsequent bubble expansion during magma ascent are primary driving forces of volcanic eruption. As such, the pre-eruptive behaviour of volatiles play a central role in modulating eruption style and dynamics (e.g., Giordano et al., 2008; Cashman and Sparks, 2013; Degruyter et al., 2017; Cassidy et al., 2018).

Various petrological tools have been developed to reconstruct the volatile history of past eruptions, capturing distinct snapshots of pre-eruptive volatile concentrations. Melt inclusions are widely used to

* Corresponding author at: Department of Earth Sciences, University of Oxford, UK.
E-mail address: amdemichaelz@gmail.com (A.Z. Tadesse).

https://doi.org/10.1016/j.chemgeo.2026.123362
Received 3 January 2026; Received in revised form 28 February 2026; Accepted 8 March 2026
Available online 10 March 2026

directly measure dissolved volatiles at different stages of magma evolution; however, they can be compromised by diffusive volatile loss or gain, often through the host crystal, as well as by post-entrapment crystallization (e.g., Qin et al., 1992; Danyushevsky et al., 2002; Portnyagin et al., 2008; Gaetani et al., 2012; Reubi et al., 2013; Preece et al., 2014). Volatile migration into shrinkage bubbles (Moore et al., 2015) may further alter the primary melt signal. In some cases, melt inclusions are only hosted in phases that are prone to leakage or are too small for reliable detection (e.g., Kent, 2008; Lloyd et al., 2013). As a result, melt inclusion data may not always represent complete or accurate records of pre-eruptive volatile abundances.

An alternative archive of magmatic volatile concentrations is provided by the phosphate mineral apatite, a common accessory phase in volcanic systems (Piccoli and Candela, 2002; Webster and Piccoli, 2015). Apatite incorporates all major volatile species (i.e., F, Cl, H_2O, S, and CO_2) into its crystal structure (e.g., McCubbin et al., 2015; Riker et al., 2018), and its compositions can be used to infer magmatic volatile budget. This is achieved through experimentally derived partitioning data (e.g., Candela, 1986; Webster et al., 2009; McCubbin et al., 2015; Li and Hermann, 2015; Li and Hermann, 2017), and thermodynamic modelling (Li and Costa, 2020). A key advantage of apatite is that phenocryst-hosted inclusions can preserve their pre-eruptive compositions under conditions where melt inclusions may have re-equilibrated (e.g., Stock et al., 2016; Stock et al., 2018). Numerous studies have used apatite to constrain compositions of fluids/melts and reconstruct volatile histories in diverse magmatic systems (e.g., Boyce and Hervig, 2009; Stock et al., 2016; Stock et al., 2018; Li et al., 2021; Humphreys et al., 2021).

In this study, we analyse the composition of apatite and glass (matrix and melt inclusions) in pumice samples from the Tullu Moye and Boset-Bericha volcanic centres, to investigate the volatile behaviour in their magmatic systems. These peralkaline volcanoes, located in the central Main Ethiopian Rift, were selected because their tephra samples host apatite and melt inclusions (Fontijn et al., 2018; Tadesse et al., 2023). We present new major, trace, and volatile element data from apatite and melt inclusions from four explosive eruptive products: younger Tullu Moye pumice (YTMP) and older Tullu Moye pumice (OTMP) at Tullu Moye (Tadesse et al., 2022; Tadesse et al., 2023), and unit #5 and #6 at Boset-Bericha (Fontijn et al., 2018). Volatile concentrations in the melt are measured in melt inclusions and estimated based on apatite mineral

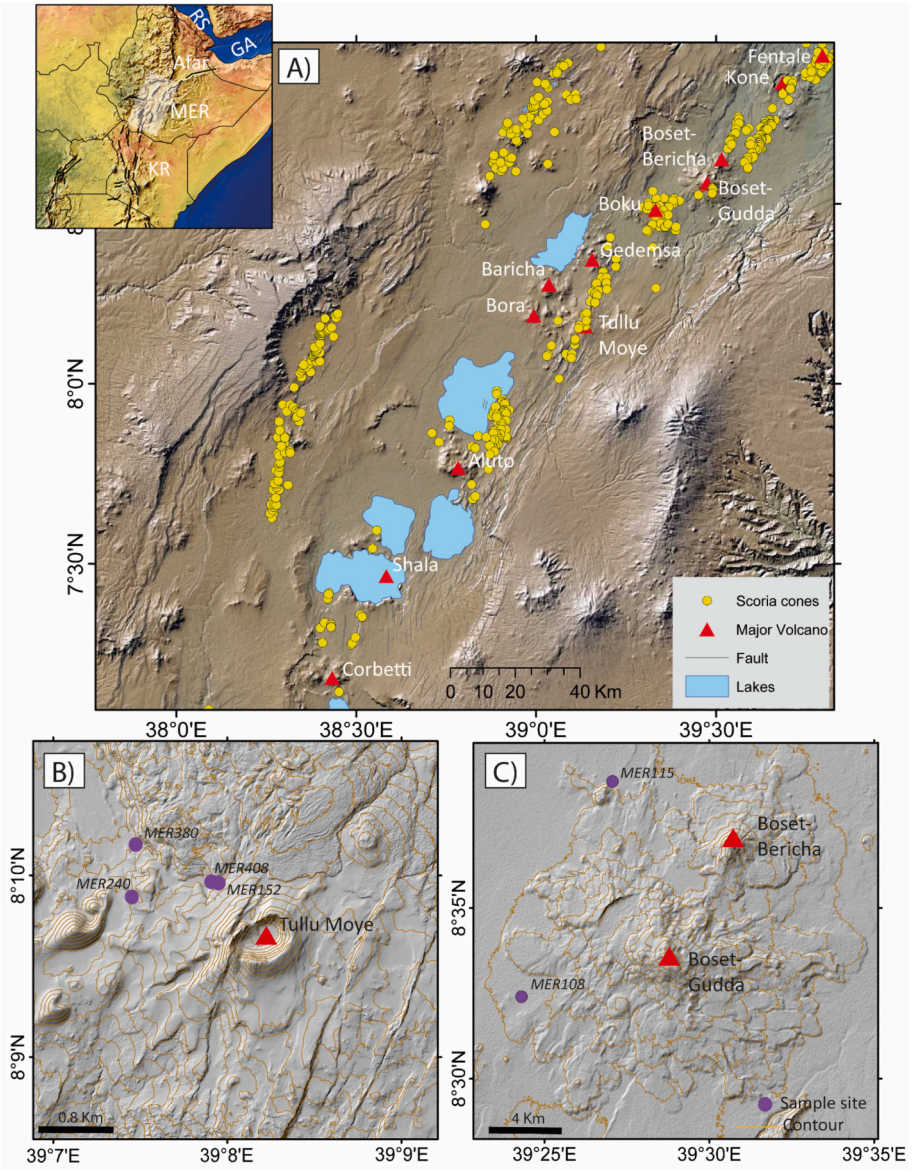

Fig. 1. (A) Overview map of the northern and central sector of the Main Ethiopian Rift (MER) that extends from the Kenyan Rift (KR) through to Afar in northeast Africa (inset), highlighting the locations of (B) Tullu Moye and (C) Boset volcanoes.

composition, and volatile evolution trends are modelled using established thermodynamic frameworks. These results are used to constrain the volatile content and evolution of peralkaline magmas in extensional settings.

2. Geological setting

The Main Ethiopian Rift (MER) represents the northernmost sector of the East African Rift System and is a mature continental rift that links the large fault-bounded grabens of the Kenyan Rift with incipient seafloor spreading in the Afar region (Fig. 1). In the MER, tectonic strain is primarily accommodated through magmatic intrusions and localised faulting within ~20 km-wide and ~ 60 km-long axial magmatic segments (Wonji Fault Belt; Ebinger and Casey, 2001; Casey et al., 2006). This structural pattern is especially well developed in the northern and central sectors of the rift, where rifting initiated around 11 Ma and 5–6 Ma, respectively (Wolfenden et al., 2004; Bonini et al., 2005). Around 1.6–2 Ma, tectonic and volcanic activity had become increasingly focused within the rift floor, establishing the present-day structural configuration (Boccaletti et al., 1999; Chernet et al., 1998; Corti, 2009). Recent volcanic activity in the rift floor is characterized by lava flows and pyroclastic deposits erupted from fissures, scoria cones, and large central volcanoes. These central volcanoes, which predominantly include calderas, are systematically aligned along the axial zone of the rift (Fig. 1). Among them, Tullu Moye and Boset are the two prominent volcanoes located in the transition zone between the central and northern MER sectors and are the focus of this study.

Tullu Moye volcano is located in a highly faulted region where the Wonji Fault Belt converges toward the eastern rift margin (Fig. 1). The volcanic edifice comprises trachytic lava flows and hydrothermally altered pyroclastic deposits. Two explosive eruptions have been identified at the volcano, producing the OTMP and YTMP deposits (TM-P1 and TM-P2, respectively in Tadesse et al., 2022). These deposits are distributed mainly to the west of the edifice, with YTMP being more spatially extensive than the more localised OTMP. Whole rock and glass chemical analyses indicate that these pumices and the obsidian lavas erupted at Tullu Moye are comenditic rhyolite in composition (Fontijn et al., 2018; Tadesse et al., 2022; Tadesse et al., 2023). The surrounding plains to the northwest and southwest are covered by thick obsidian and basaltic lava flows, as well as scoria, spatter, and cinder cones. These products were erupted along NNE-SSW-trending fissures and partially obscure older tephra deposits from the volcano. An obsidian flow located north of the main edifice, possibly erupted during historical time (ca. 1900 CE), and covers an area of approximately 2.7 × 1.6 km. However, there are no detailed eruption records or precise age constraints currently available for this modern eruption (Gouin, 1979).

The Boset volcanic complex lies approximately 60 km northeast of Tullu Moye and is one of the largest stratovolcanoes in the MER. It comprises two main centres, Bericha and Gudda, which are aligned along a NNE-SSW-trending lineament parallel to the Wonji Fault Belt. The southern and largest edifice, Boset-Gudda, hosts a 2.5 km-wide arcuate ridge on its northwestern flank, interpreted as the remnant of largely infilled caldera that formed after 119.8 ± 6.1 ka (Di Paola, 1972; Siegburg et al., 2018). Boset-Bericha, located to the north, is thought to have developed around the same time as Gudda and is characterized by multiple phases of lava flow emplacement (Brotzu et al., 1980). Both edifices are dominated by thick trachytic and peralkaline rhyolitic lava flows with associated pyroclastic deposits (Macdonald et al., 2012). These silicic lava flows often originated from breached cones, with runout distances extending up to 11 km from their vents (Siegburg et al., 2018). On the western flank of the Boset complex, road cuts and dry river gullies expose stratigraphic sections containing up to six pyroclastic fall deposits that are interbedded with palaeosols, and presumably of Late Pleistocene – Holocene age (Fig. 2; Fontijn et al., 2018). The uppermost and most voluminous and widespread of these deposits is the Boset pumice. The top three pumice fall units have pantelleritic rhyolite compositions and are likely sourced from the Boset-Gudda centre (Siegburg et al., 2018; Fontijn et al., 2018). In contrast, the basal two pumice fall units (i.e., Unit #5 and Unit #6), which occur in distinct stratigraphic sections (MER108 and MER115; Figs. 1 and 2), are comenditic rhyolite in composition (Fontijn et al., 2018). Since comenditic lava flows are known only from the Bericha edifice, these lower pumice deposits are inferred to have originated from the Boset-Bericha centre (Siegburg et al., 2018; Fontijn et al., 2018).

3. Methods

The samples utilized in this study were collected from proximal pumice deposits of explosive eruptions from Tullu Moye and Boset-Bericha volcanoes (Fig. 1). Sampling locations and further details of

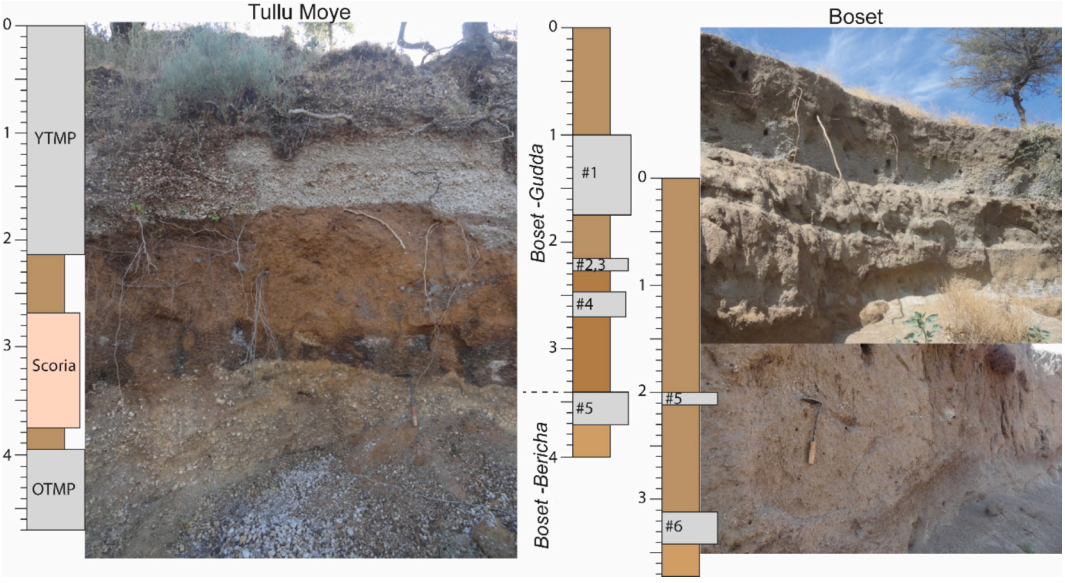

Fig. 2. Field photographs and schematic stratigraphic logs of pyroclastic deposits from Tullu Moye (YTMP: Younger Tullu Moye Pumice & OTMP: Older Tullu Moye Pumice) and Boset volcanoes (unit #6 to #1) after Tadesse et al. (2022) and Fontijn et al. (2018). Note that the complete stratigraphy of Boset eruption sequence is inferred from multiple stratigraphic sections.

the deposits are reported in Tadesse et al. (2022, 2023) or Fontijn et al. (2018). A total of 13 samples were selected for this study from stratigraphic units across these volcanic systems. Apatite-bearing Tullu Moye samples include both older and younger pumice units, and units #5 and #6 from Boset-Bericha were selected to enable a comparative study.

Samples were gently crushed, and clinopyroxene phenocrysts containing apatite and melt inclusions were handpicked from the 0.25 to 2 mm size fraction. Crystals were mounted in epoxy and polished to expose apatite and melt inclusion sections for microanalysis. These polished sections were examined under reflected light microscopy and via backscattered electron imaging using a FEI Quanta 650 Scanning Electron Microscope (SEM) at the Department of Earth Sciences, University of Oxford. Apatite crystals and melt inclusions suitable for analysis were identified with their host minerals. The textural context of apatite inclusions (e.g., fully vs. partially enclosed) was noted to evaluate potential compositional variability. Melt inclusions were analysed only if they did not show visual signs of post-entrapment crystallization and were located away from cracks in the host phenocryst.

Major, trace, and halogen element compositions in minerals and glass were measured using a JEOL JXA-8200 electron microprobe (EPMA) at the Research Laboratory for Archaeology and the History of Art, University of Oxford. Prior to the EMPA analysis, samples were re-polished to remove any compositional modification caused by SEM electron-beam exposure (Stock et al., 2015), and then carbon-coated along with appropriate secondary standards. Volatile elements (i.e., F, Cl and S) in apatite were measured with a defocused 7 μm beam at 15 kV and 10 nA, with halogens measured first to reduce the effects of beam damage. Major and trace elements in apatite (i.e., Si, Na, Mg, La, Ce, P, Ca, Fe and Mn) were analysed using the same beam size and voltage but at a higher current (35 nA). Where possible, apatite crystals were analysed with their c-axis parallel to the plane of the mount to minimize the effect of time-dependent halogen migration (Stormer and Pierson, 1993; Goldoff et al., 2012; Stock et al., 2015).

Glass compositions were measured using a defocused 10 μm beam at 15 kV and 6 nA to minimize alkali element migration (e.g., Humphreys et al., 2006). Volatile elements (F, Cl, and S) in glass were measured separately in a second analysis using a 30 nA current. Clinopyroxene from Boset-Bericha were analysed with a defocused 3 μm beam at 15 kV and 40 nA. Clinopyroxene data for Tullu Moye samples were taken from Tadesse et al. (2023). For both minerals and glass, count times were 10–30 s for major elements and 30–90 s for minor elements. In apatite, longer count times were applied for certain elements to improve precision: 120 s for F; and 140 s for Mg, Cl, and SO_3. Backgrounds were determined by counting for half of the on-peak count time on either side of the peak. Analyses with totals <92% or > 102% in glass and apatite were discarded. Analytical accuracy and precision were assessed through repeated measurements of well-characterized minerals and glasses, including Durango and Wilberforce apatites; StHs6/80-G, ATHO-G and GOR132-G MPI-DING reference glasses (Jochum et al., 2006); and Pyrope and Hornblende (Smithsonian; Jarosewich et al., 1980) for clinopyroxene analyses. Results showed good agreement with published reference values (see Supplementary Tables 1 to 4).

A subset of apatite and glass samples was analysed for H, C, F, and Cl using Secondary Ion Mass Spectrometry (SIMS) on the Cameca ims 7f-Geo instrument at the Edinburgh Ion Microprobe Facility, following the procedures described in Riker et al. (2018). Additional elements, including Na, Mg, Si for apatite and Mg and Al for melt inclusions were measured to allow comparison with EMPA data. For apatite analyses, Fe and Ti were included to monitor overlap of the ion beam with the mineral host. Prior to SIMS analysis, samples were re-polished, cleaned with ethanol, coated with gold, and loaded into the SIMS at least 12 h before analysis. For apatite, concentrations of SiO_2, MgO, Na_2O, F, Cl, C, and H_2O were calculated from working curves of $^{30}Si/^{44}Ca$ vs SiO_2, $^{25}Mg/^{44}Ca$ vs MgO, $^{23}Na/^{44}Ca$ vs Na_2O, $^{19}F/^{44}Ca$ vs F, $^{35}Cl/^{44}Ca$ vs Cl, $^{12}C/^{44}Ca$ vs C, and $^{1}H/^{44}Ca$ vs H_2O. These curves populated by using independently characterized apatite standards (see Anenburg et al., 2025 for compositions). For glass, concentrations of MgO, F, Cl, CO_2, and H_2O, normalized to SiO_2 based on EMPA of same analytical spots, were similarly derived from working curves of $^{25}Mg/^{30}Si$, $^{19}F/^{30}Si$, $^{35}Cl/^{30}Si$, $^{12}C/^{30}Si$, and $^{1}H/^{30}Si$, respectively. These were calibrated using well-characterized glass standards for CO_2 and H_2O (Shishkina et al., 2010) and Lipari glass for F and Cl. Working curves were generated at the beginning of each analytical session. SIMS background counts were monitored using anhydrous glass for melt inclusions, while no background correction was applied to apatite.

4. Results

4.1. Petrography and mineral chemistry

The rhyolitic pumice samples from Tullu Moye and Boset-Bericha are vesicular and holocrystalline to glomeroporphyritic in texture (Ronga et al., 2010; Tadesse et al., 2023). They exhibit a mineral assemblage composed of phenocrysts of alkali feldspar, plagioclase feldspar, clinopyroxene, and minor Ti-magnetite set in a glassy groundmass. Clinopyroxene phenocrysts from the older eruptive units of Tullu Moye and Boset-Bericha commonly display resorption textures, such as irregular crystal faces and pervasive cracking. In contrast, clinopyroxenes from younger deposits generally have well-formed, euhedral crystal faces (Fig. 3). The compositions of the clinopyroxenes plot near the augite and diopside-hedenbergite boundary, with enrichment in Fe and Mg toward younger stratigraphic units (Fig. 4). Specifically, Fe contents range from $Fs_{33–44}$ in YTMP and Boset #5 to $Fs_{14–39}$ in OTMP and Boset #6. Corresponding Mg contents span $En_{15–28}$ in YTMP and Boset #5, and $En_{22–44}$ in OTMP and Boset #6. Clinopyroxenes from Tullu Moye are more calcic ($Wo_{40–44}$) than those from Boset-Bericha ($Wo_{37–42}$).

Clinopyroxene macrocrysts host inclusions of apatite, melt, and Ti-magnetite (Fig. 3). Apatite crystals, typically <200 μm in size, occur as microphenocrysts fully or partially enclosed in the matrix glass or as inclusions within other phenocryst phases such as clinopyroxene and Ti-magnetite. These different textural occurrences, may reflect different stages of equilibration with the surrounding melt. A notable inclusion relationship is observed where Ti-magnetite, itself included in clinopyroxene phenocrysts, hosts apatite inclusions relatively smaller in size (< 50 μm) than those occur within the clinopyroxene. The apatites commonly exhibit an acicular habit and some display a slightly offset central cavity partially filled with glass. Melt inclusions are <300 μm in diameter, predominantly sub-spherical, glassy, and free of post-entrapment crystallization or shrinkage bubbles. Most melt inclusions are entirely enclosed within clinopyroxene phenocrysts, although a few are located near cleavage planes of the host mineral and these were not analysed.

4.2. Glass compositions

The glass analyses presented include both matrix glasses (Fontijn et al., 2018; Tadesse et al., 2022) and melt inclusions hosted in clinopyroxene phenocrysts. The supplementary datasets from Fontijn et al. (2018) and Tadesse et al. (2022) are reported with the new data in Supplementary Tables 2 and 3. Both matrix glass and melt inclusions span a compositional range of 65.92–77.39 wt% SiO_2 and 7.7–12.4 wt% $Na_2O + K_2O$, plotting predominantly within the rhyolite field on the Total Alkali-Silica (TAS) diagram (Le Bas et al., 1986), with a few samples straddling the trachyte-trachydacite boundary (Fig. 5). All glasses have peralkaline rhyolitic compositions, with peralkalinity index ($PI = mol\ [Na_2O + K_2O]/Al_2O_3$) ≥ 1. Based on the classification scheme of Macdonald (1974), the peralkaline glasses are all comendite, characterized by 8.97–16.36 wt% Al_2O_3 and 1.67–7.06 wt% FeO (Fig. 5). Matrix glasses from the YTMP and Boset-Bericha pumices display significant compositional differences to melt inclusions, particularly showing higher SiO_2 (> 73 wt%) and Na_2O (> 6 wt%). Additionally, major elements such as K_2O against SiO_2 have a different trend for the

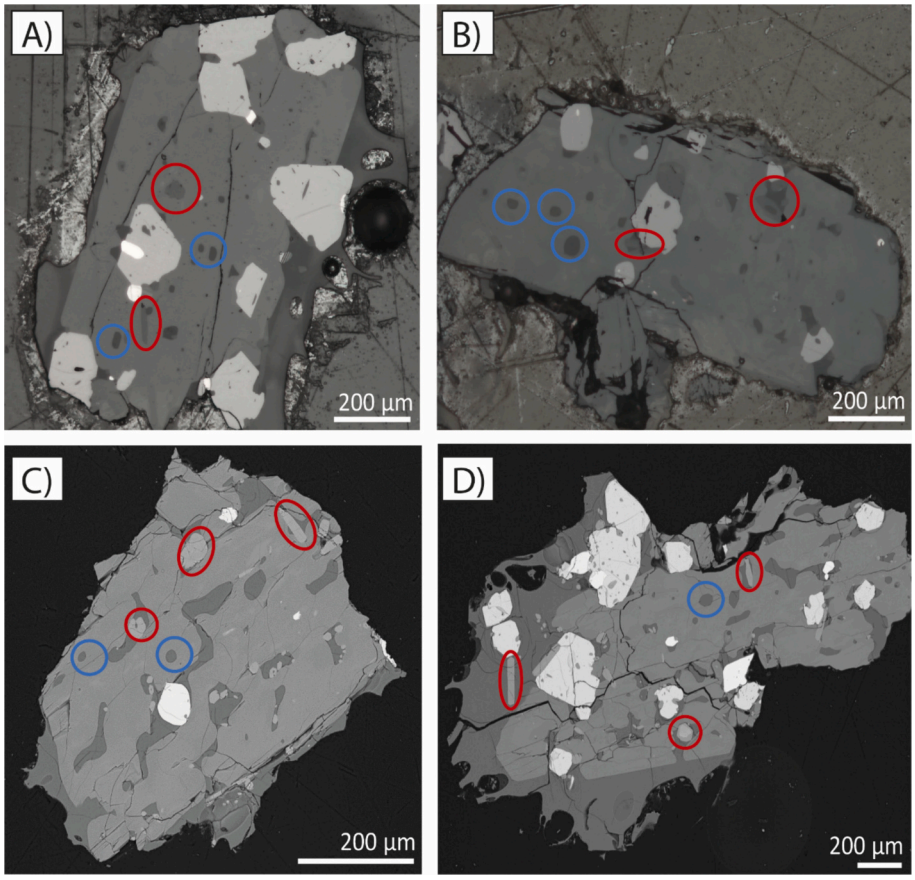

Fig. 3. Representative reflected light (A & B) and back-scattered electron (BSE) SEM images (C & D) showing typical occurrences of apatite and melt inclusions within clinopyroxene phenocrysts from pumice samples of Tullu Moye and Boset-Bericha deposits. Analysed apatite and melt inclusions are indicated by blue and red circles, respectively. (For interpretation of the references to colour in this figure legend, the reader is referred to the web version of this article.)

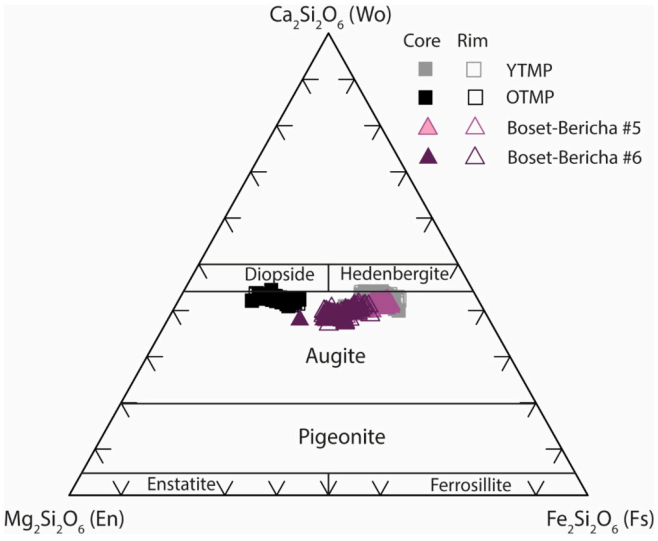

Fig. 4. Compositions of pyroxene phenocrysts from Tullu Moye (YTMP & OTMP) and Boset-Bericha (unit #5 and #6) plotted on the classification diagram of Morimoto (1988). Pyroxene dataset for Tullu Moye is from Tadesse et al. (2023).

matrix glasses compared to the melt inclusions. However, the OTMP matrix glasses and their corresponding melt inclusions exhibit overlapping major element compositions.

The glasses display a continuous compositional trend and exhibit systematic major element variations (Fig. 6). With increasing SiO_2, concentrations of CaO, MgO, FeO, and MnO generally decrease, while K_2O increases. Al_2O_3 and TiO_2 contents rise to ~16 wt% Al_2O_3 and ~ 0.5 wt% TiO_2 before falling to ~13 wt% Al_2O_3 and < 0.2 wt% TiO_2 in the more silicic end. Some major elements in the matrix glass such as FeO, MnO, MgO, and CaO display relatively restricted compositional ranges and remain nearly constant at the high SiO_2 end. Notably, OTMP glasses follow a distinct evolutionary trend in MgO and CaO versus SiO_2 binary diagrams, marked by relatively higher MgO and CaO contents. Additionally, OTMP glasses have consistently lower Na_2O concentrations than those from YTMP and Boset-Bericha.

Major element analytical totals are high in all analysed glasses (>92 wt%; Supplementary Tables 2 and 3), which may indicate low concentrations of dissolved volatiles. Matrix glasses contain up to 0.36 wt% Cl, although most samples exhibit significantly lower concentrations (0.17 ± 0.04 wt%, Fig. 7). Variations in Cl with SiO_2 broadly mirror those of TiO_2, with increasing concentrations followed by a decline in the most evolved compositions (Figs. 6 and 7). Along this trend, OTMP glasses generally show higher Cl contents than those from YTMP and Boset-Bericha. Fluorine concentrations were consistently below detection limits in the EMPA dataset, except in one OTMP glasses where F reaches up to ~0.1 wt%. In contrast, SIMS analyses show F contents ranging from 0.05 to 0.21 wt%, with melt inclusions from OTMP pumice yielding significantly lower values (< 0.09 wt%) compared to those from other eruptive units considered in this work (0.14–0.21 wt%). Only a few glasses had sulphur concentrations above the detection limit, with values reaching ~0.01 wt% SO_3. Melt inclusions typically contain ~2.09–4.33 wt% H_2O, and CO_2 concentrations are minimal across the dataset, reaching up to 700 ppm. For comparison, matrix glass shows up

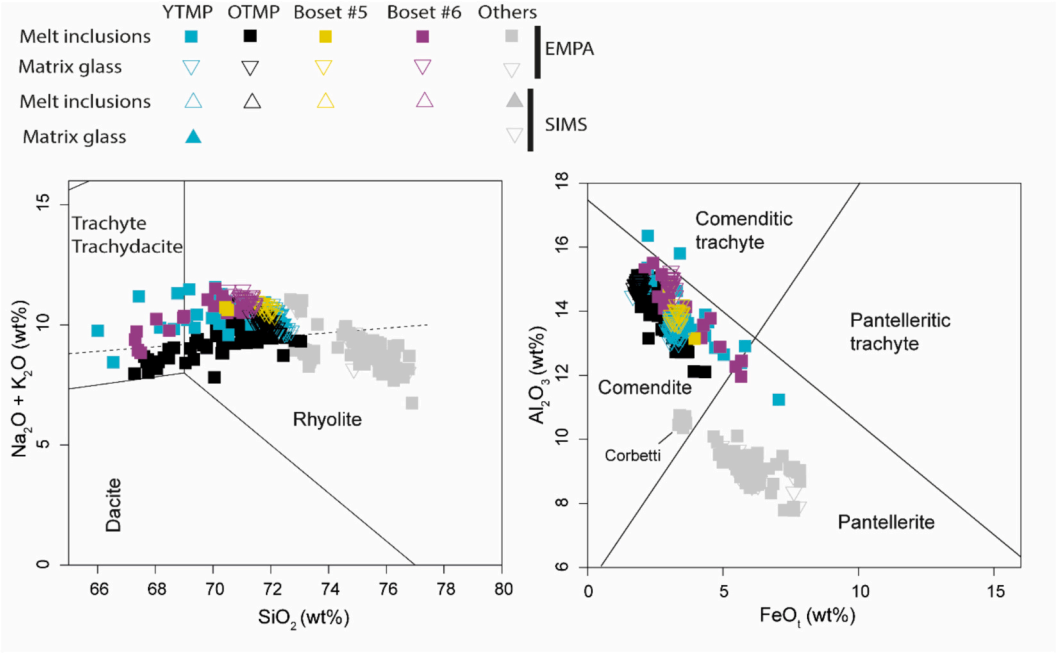

Fig. 5. Melt inclusion and matrix glass compositions plotted on the Total Alkali vs. Silica diagram (TAS; Le Bas et al., 1986), and peralkaline rhyolite and trachyte classification diagram (Macdonald, 1974). Matrix glass data for Tullu Moye and Boset-Bericha are from Tadesse et al. (2022) and Fontijn et al. (2018), respectively. Evolved melt data from other volcanoes in the MER (Kone, Aluto, Fentale and Corbetti; Fig. 1a) have been plotted for comparison (data from Iddon and Edmonds, 2020).

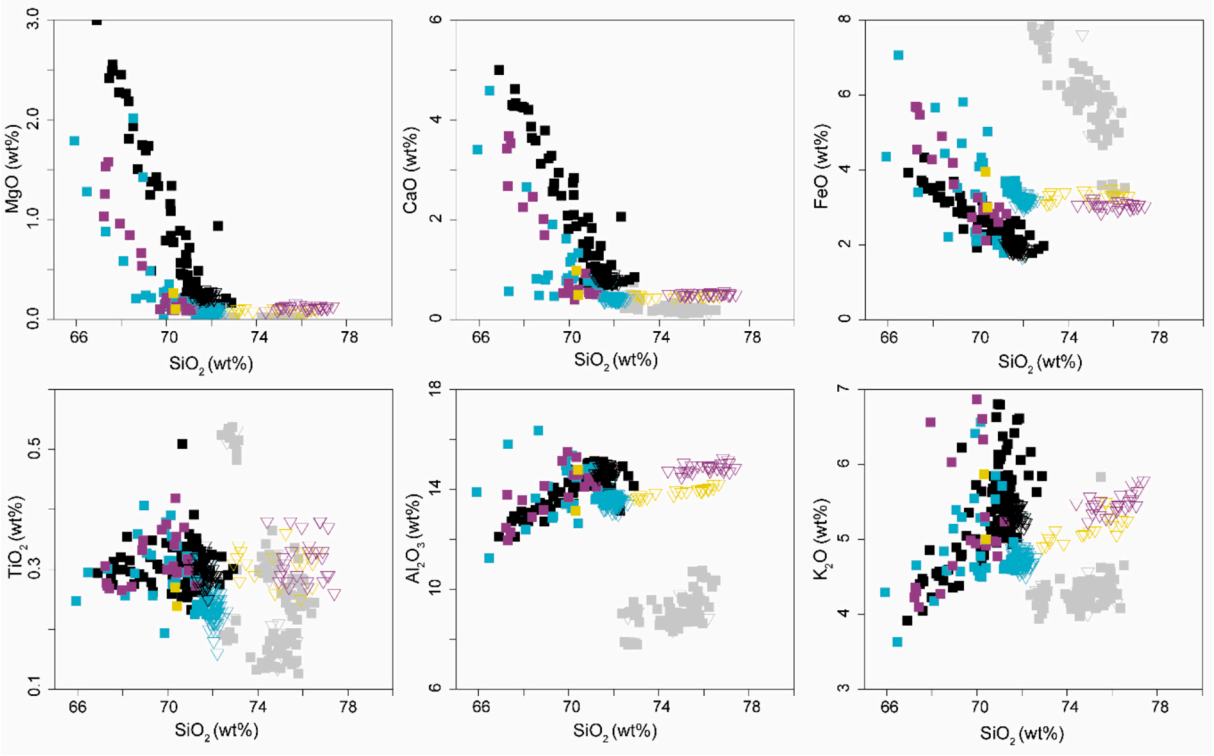

Fig. 6. Major element variation diagrams for melt inclusions and matrix glasses from Tullu Moye and Boset-Bericha. Matrix glass data for Tullu Moye and Boset-Bericha are from Tadesse et al. (2022) and Fontijn et al. (2018), respectively. Data for other evolved eruptions is from Iddon and Edmonds (2020). Symbols and colours are same as Fig. 5.

to 0.22 wt% Cl, ~0.13 wt% F, ~1 wt% H_2O, and < 11 ppm CO_2.

4.3. Apatite compositions

A total of approximately 350 EMPA analyses were conducted on 165 grains to characterize the chemical compositions of apatites

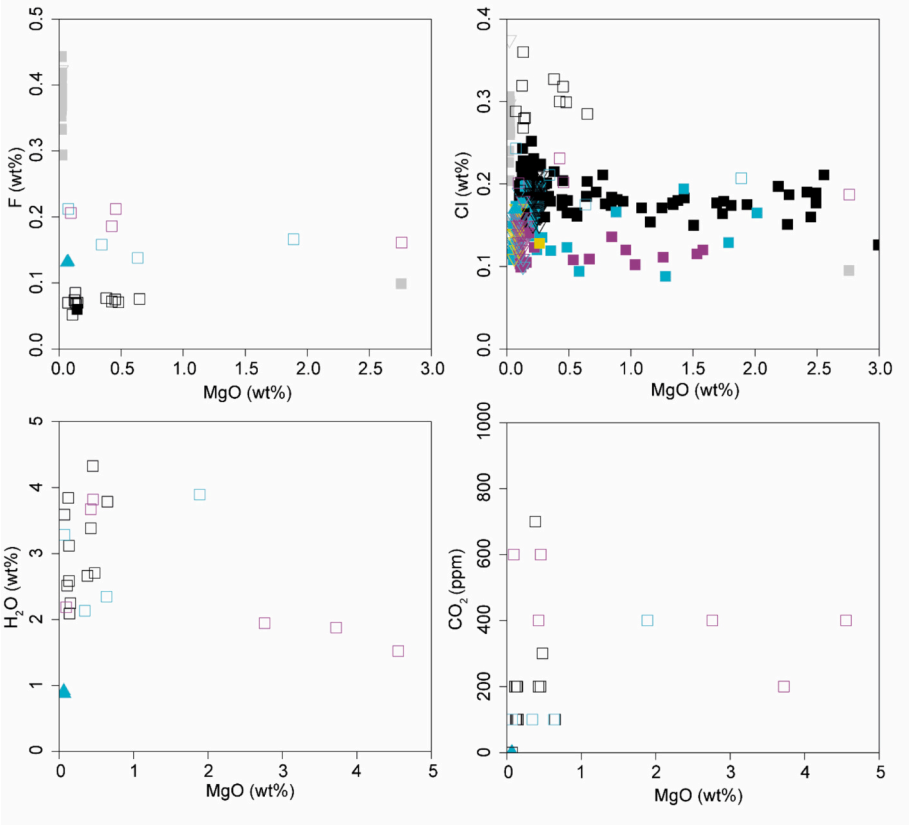

Fig. 7. Volatile element variation diagrams of melt inclusions from Tullu Moye and Boset-Bericha comenditic eruptions. Symbols and colours are same as Fig. 5.

(Supplementary Table 4). Apatite crystals from both Tullu Moye and Boset-Bericha are typically fluorapatite, exhibiting F and Cl contents of ≤3.8 wt% and 0.05–0.76 wt%, respectively. Additionally, significant concentrations of minor and trace elements are present, including 0.26–3.57 wt% FeO, ≤ 0.73 wt% MgO, 0.13–0.28 wt% MnO, 0.14–4.32 wt% SiO_2, and up to 0.058 wt% SO_3. The rare earth elements such as La_2O_3 (0.18–0.98 wt%) and Ce_2O_3 (0.49–2.34 wt%) are also relatively enriched (Fig. 8). Apatite grains are compositionally homogeneous with respect to halogen and trace elements, based on multiple spot analyses across individual grains. No systematic variation in halogen or trace element concentrations was identified between apatite hosted in clinopyroxene, Ti-magnetite, or those occurring as microphenocrysts. However, microphenocrystic apatite consistently displays the lowest halogen concentrations, while apatite inclusions within Ti-magnetite generally exhibit higher FeO contents than in other textural settings, more likely resulted from secondary fluorescence effects (e.g., Llovet et al., 2020).

Hydroxyl (OH) concentrations were calculated for the EMPA dataset by assuming that the vacancy at the X-site is filled by OH after considering the amount of Cl and F. We used the method described by Ketcham (2015) to calculate the apatite mineral formula on a 25-oxygen basis, which accounts for the OH content that cannot be directly analysed by EPMA. Because F, Cl, and OH share the same structural site in apatite, results are plotted in a ternary F-Cl-OH diagram, with the majority of the data falling in the field of volcanic apatite (Li and Costa, 2020; Fig. 9). The calculated mole fraction ratios range from 0.01 to 2 X_{Cl}/X_{OH}, ≤ 98 X_F/X_{OH}, and ≤ 99 X_F/X_{Cl}, where X_F, X_{Cl}, and X_{OH} represent the mole fractions of F, Cl and OH, respectively.

SIMS analyses performed on larger apatite grains yielded halogen and trace element concentrations that closely overlap with those obtained by EPMA. Additionally, SIMS provided H_2O and CO_2 contents ranging from 0.24–0.74 wt% and 0.007–0.4 wt%, respectively.

Fig. 9 illustrates two distinct trends along the F-OH exchange line with data points mainly falling toward the high-F end, primarily separated by differences in Cl content. Apatite from the OTMP displays significantly higher Cl concentrations (0.6–0.8 wt%), whereas apatite from the YTMP and Boset-Bericha (≤0.1 wt%) eruptions falls along a low-Cl trend. These two linear trends are further evident in binary plots of X_F/X_{OH} vs. X_{Cl}/X_{OH} and X_F/X_{Cl} vs. X_{Cl}/X_{OH}, all showing positive correlations. Notably, OTMP apatite defines a distinct evolutionary lineage with steeper (nearly sub-vertical) slopes, attributed to its higher X_{Cl}/X_{OH} and lower X_F/X_{Cl} and X_F/X_{OH} ratios. The second major trend, defined by lower X_{Cl}/X_{OH} and higher X_F/X_{OH}, is predominantly formed by apatites from YTMP and Boset-Bericha eruptive units. Apparent trends marking small differences in X_F/X_{Cl} in Fig. 9b-d result from reaching the limit of resolution in ultra-low chlorine apatites. We therefore do not attempt to model the YTMP and Boset-Bericha eruptions. In addition to halogen contents, notable compositional differences exist in other volatile and trace elements. Specifically, OTMP apatite is characterized by higher in H_2O and lower F, MgO, and MnO relative to the YTMP and Boset-Bericha apatite, which show substantial compositional overlap.

5. Discussion

5.1. Magmatic volatiles in silicic melts from apatite composition

The melt inclusions studies in the MER show extensive degassing as we can learn from previous works (e.g., Iddon and Edmonds, 2020; Wong et al., 2023). To estimate the primitive melt volatile content various methods have been used, including volatile to non-volatile elements ratios (Iddon and Edmonds, 2020; Wong et al., 2023). These methods have wide uncertainty on the assumptions on the volumes of melt intruded into the crust. Hydrous minerals such as apatite have been utilized as proxies for constraining magmatic volatiles (e.g., Piccoli and Candela, 1994; Boyce and Hervig, 2009; Douce et al., 2011). Several studies (e.g., Boyce et al., 2014; Li and Hermann, 2015; McCubbin et al.,

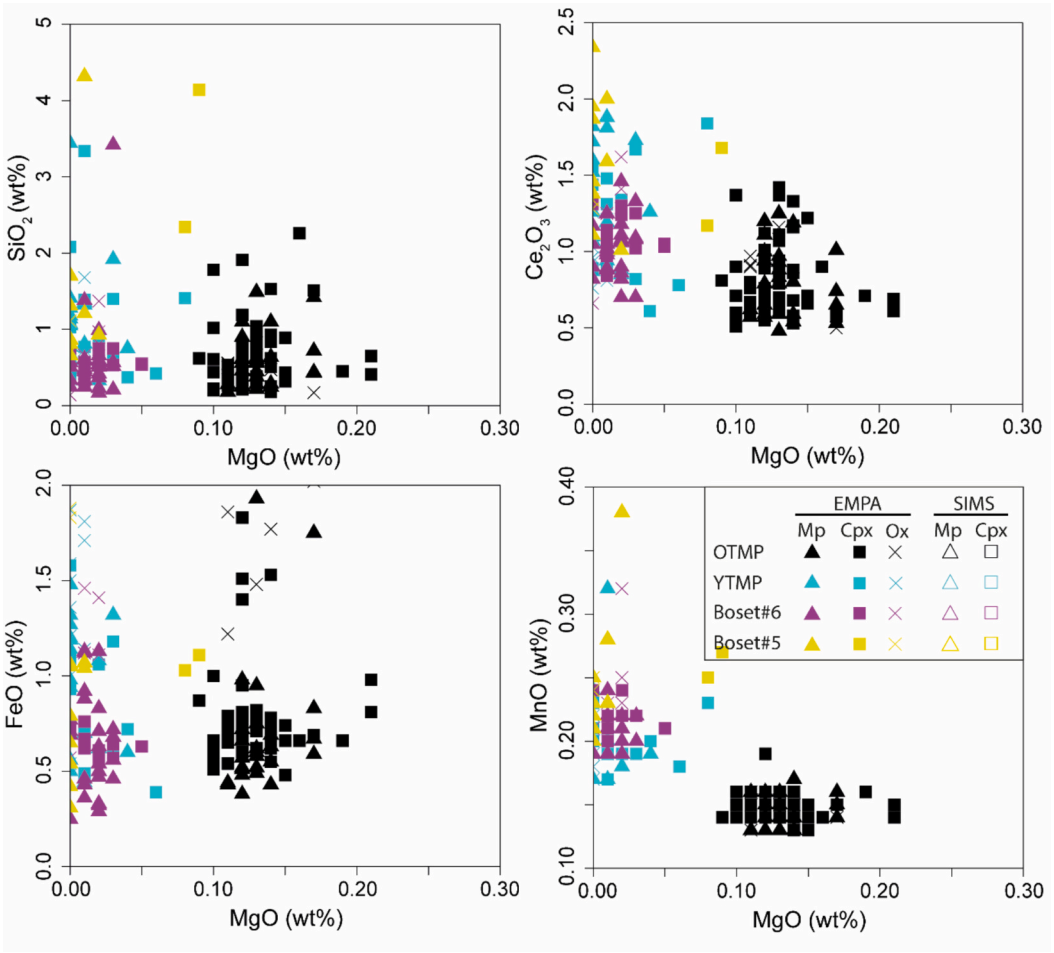

Fig. 8. Trace element variation diagrams of apatite from Tullu Moye and Boset-Bericha. Mp: apatite microphenocrysts, and the other apatites analysed were either hosted in clinopyroxene (cpx) or oxides.

2015) have demonstrated that simple Nernst partition coefficients between apatite and melt are inadequate for estimating volatile concentrations in the melt. This is because Cl, F, and OH occupy the same crystallographic site in the apatite structure, and their incorporation is governed by stoichiometry and crystallization conditions (e.g., temperature and pressure), rather than by melt composition alone (Li and Costa, 2020). In this study, we apply recently calibrated thermodynamic models for apatite-melt partitioning (e.g., Li and Hermann, 2017; Li and Costa, 2020) to estimate the concentrations of Cl, F, H_2O, SO_3, and CO_2 in silicic melts based on apatite compositions. We then applied the coupled fractional crystallization-degassing model of Lormand et al. (2024) to the population of apatite data from OTMP, in order to investigate the overall behaviour of volatiles during evolution of the whole magmatic system.

Melt Cl and F concentrations were first estimated independently from apatite using the thermodynamic model of Li and Hermann (2017), with required input parameters such as melt composition and apatite crystallization temperature derived from glass chemistry and thermobarometric calculations. Temperatures for apatite inclusions were constrained using clinopyroxene-only thermometry (Jorgenson et al., 2022; ± 47.6 °C uncertainty), while those for microphenocrystic apatites were inferred using matrix glass compositions and the calibration of Weber and Blundy (2024, ± 21 °C uncertainty), following the approach outlined in Li and Costa (2020). The resulting temperatures (i.e., 845–870 °C) broadly overlap with apatite saturation temperatures (782–852 °C) derived from the empirical model of Piccoli and Candela (1994), and are considered representative of apatite crystallization within the magma. These values are higher than melt temperatures inferred from feldspar-liquid thermometry (700–765 °C, Tadesse et al., 2023), which likely record later or different stages of magma evolution rather than the conditions of apatite formation. Using this method, we estimate melt concentrations of OTMP (0.15–0.73 wt% Cl and 0.05–0.86 wt% F), YTMP (0.03–1.18 wt% Cl and 0.33–5.19 wt% F), Boset-Bericha unit #5 (0.04–0.57 wt% Cl and ≤ 0.47 wt% F), and Boset-Bericha unit #6 (0.04–0.65 wt% Cl and 0.45–5.88 wt% F, Supplementary Table 4). The uncertainty related to temperature selection may affect the estimates by up to ~0.1 wt%. Melt H_2O concentrations were estimated using the thermodynamic F-Cl-OH partitioning model of Li and Costa (2020). Similar temperature constraints and methodological approaches were applied as for the melt F and Cl estimation. The resulting H_2O contents are 0.32–5.16 wt% for OTMP, 0.01–3.34 wt% for YTMP, 0.01–0.88 wt% for Boset-Bericha unit #5, and 0.03–0.94 wt% for Boset-Bericha unit #6 (Supplementary Table 4). Uncertainty in these estimates can reach up to ~2 wt%.

Similarly, the sulphur and CO_2 content in the silicate melt is calculated using apatite composition. Sulphur content in the melt was calculated by using the equation of Li et al. (2021), based on the distribution coefficient for S between apatite and silicate melt. The calculated sulphur content in the silicate melt is low in all samples, reaching 32 ppm. In order to calculate melt CO_2 content we considered distribution coefficients of Riker et al. (2018). The calculated CO_2 content in the melt is 0.04–1.14 wt% for OTMP, 0.06–0.3 wt% for YTMP, and 0.02–0.72 wt% for Boset #6.

These apatite-based volatile estimates are compared with melt inclusion data obtained in this study and those observed in other evolved melts erupted from the MER (Iddon and Edmonds, 2020). The estimated

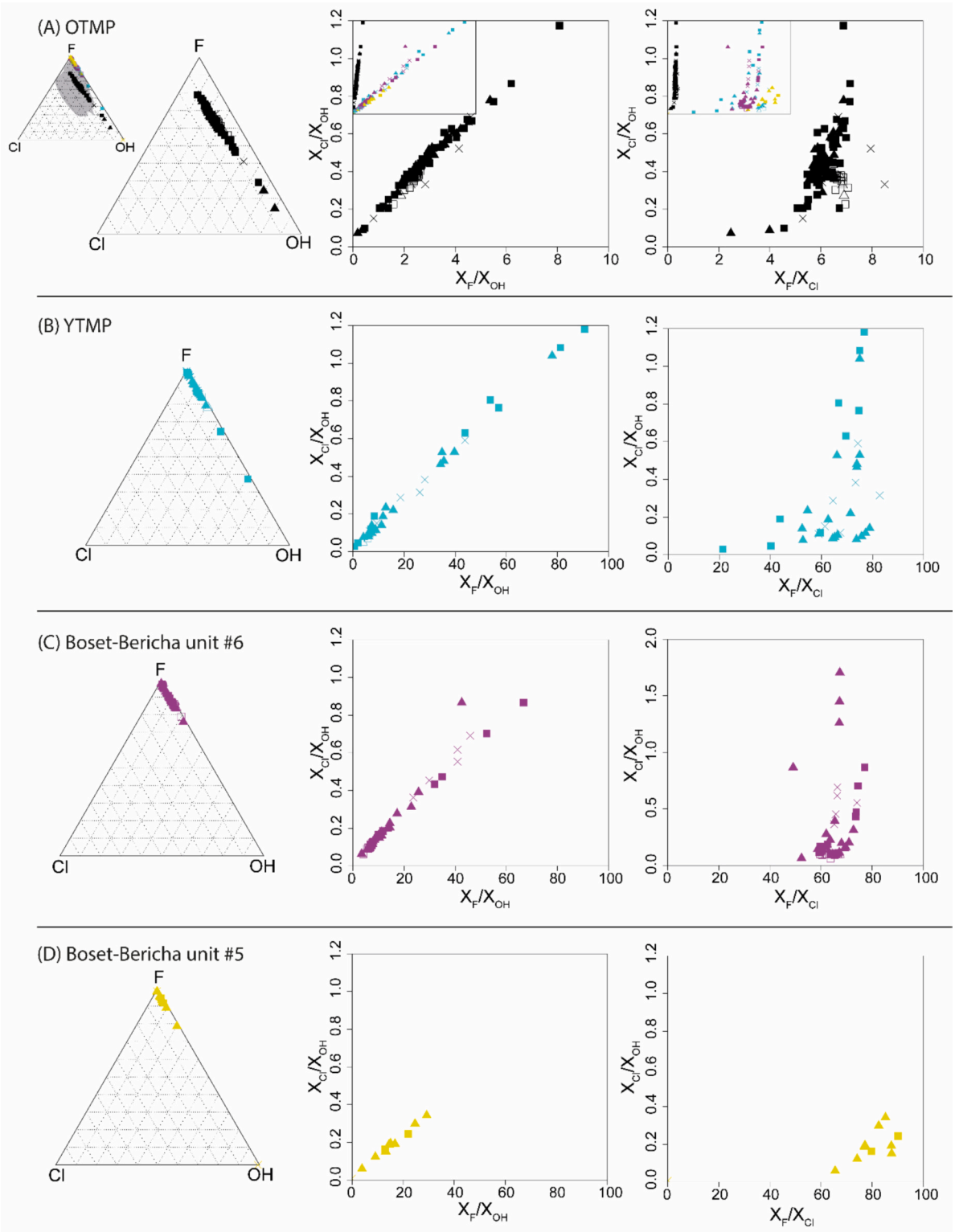

Fig. 9. Ternary and bivariate plots of apatite volatile compositions for each considered eruption. An inset shows all the apatites plotted together, and shows that the OTMP apatites span a much narrower range of X_F/X_{OH} (0–8) relative to the other samples (0−100). Grey shades show the compositional range of volcanic apatites after Li and Costa (2020).

melt Cl and SO_3 concentrations from apatite are in good agreement with melt inclusion data for all eruptive records considered. For H_2O, apatite-based values align very well with melt inclusion data from Tullu Moye samples, while values for Boset-Bericha are consistently lower and overlap only with the lower range of melt inclusion H_2O contents that still falls in the same range if we consider the error bar. A more pronounced discrepancy is observed in F and CO_2 concentrations: apatite-based estimates are systematically higher than those from melt inclusion analyses across all eruptive units. We further compare our dataset to the volatile data of Iddon and Edmonds (2020), who analysed quartz-hosted melt inclusions from Fentale, Kone, Aluto, and Corbetti pantelleritic deposits in the central and northern MER. Our measured

and estimated Cl and H_2O contents are consistent with the less evolved rhyolitic melt inclusions reported for Fentale and Corbetti (< 0.19 wt% Cl and ≤ 4 wt% H_2O), which is expected because of their similarities in composition to the studied deposits. Fluorine (< 0.38 wt%) and carbon dioxide (< 300 ppm) concentrations in their study are comparable to our melt inclusion values but remain lower than our apatite-derived estimates.

Several factors may account for the observed discrepancies in F and CO_2 concentrations between apatite-derived and those measured in melt inclusions. A key source of uncertainty for the F would be the stoichiometric calculation of OH in apatite, which influences the estimation of both OH and consequently F concentrations (e.g., Li and Costa, 2020; Dallara et al., 2023). Such uncertainties can be minimized by directly measuring H_2O and CO_2 in apatite. In our case, we used SIMS data for these calculations, as they include direct H_2O and CO_2 measurements, yielding F contents of ~0.15–0.2 wt% in the melt. These values fall within the range of F concentrations from melt inclusions, suggesting that the mismatch observed in the EMPA-derived dataset most likely reflects uncertainties associated with stoichiometric OH estimations rather than true compositional differences. In contrast, the discrepancy observed for CO_2 likely reflects a different process. In the MER, deep CO_2 degassing is commonly attributed to magmatic sources and can significantly modify melt inclusion CO_2 contents during ascent and storage (e.g., Hunt et al., 2017; Iddon and Edmonds, 2020; Wong et al., 2023). The CO_2 concentrations inferred from apatite, therefore, more likely represent primitive magmatic CO_2 contents, prior to extensive degassing.

5.2. Pre-eruptive volatile behaviour and eruption trigger

The volatile content of apatites serves as a valuable tracer of volatile evolution in magmatic systems (e.g., Piccoli and Candela, 1994; Stock et al., 2016; Stock et al., 2018; Humphreys et al., 2021). As illustrated in Fig. 9, the X_{Cl}/X_{OH} and X_F/X_{OH} ratios of apatite from Tullu Moye and Boset-Bericha comenditic deposits generally follow a linear trend, indicating minimal changes in relative F and Cl compatibility during apatite crystallization. This suggests that magmatic differentiation was the dominant control on volatile evolution, since as magma evolves it progressively increases the volatile contents of the residual melt, consistent with the increase in X_{Cl}/X_{OH} with decreasing MgO contents of apatite (Supplementary Fig. 1). Prior to volatile saturation, F, Cl, and H_2O are assumed to be incompatible in the silicate melts given the observed phase assemblage. The observed positive correlation of halogen molar ratios in Tullu Moye and Boset-Bericha apatites therefore reflects progressive fractionation. This fractionation trend is apparent in the glass data as well, with elements such as CaO and MgO showing strong negative correlations with SiO_2 (Fig. 6). Fractionation likely continued in the host melt even after the melt inclusions were trapped, as suggested by the relatively lower SiO_2 and Na_2O contents in melt inclusions compared to the matrix glass. A subset of apatites exhibiting anomalously high Cl and F (i.e., $X_{Cl}/X_{OH} > 0.9$ and $X_F/X_{OH} > 40$, Figs. 5 and 6) likely record late-stage processes such as cooling, or may have been scavenged from fragments of older crystalline material incorporated during eruption (cf. Humphreys et al., 2021; Stock et al., 2018).

In order to investigate the effect of differentiation on volatiles, and to determine the timing of fluid exsolution during fractionation, we tested whether textural constraints can provide a temporal framework to the apatite dataset (e.g., Stock et al., 2016; Stock et al., 2018). However, the close compositional match between groundmass-hosted and inclusion-hosted apatite suggests relatively early apatite saturation and minimal re-equilibration (e.g., Chelle-Michou and Chiaradia, 2017). A few microphenocrysts extend to lower volatile contents, suggesting some evidence of re-equilibration with melt during prolonged contact. Apatite Cl concentrations from YTMP and Boset-Bericha are too low to model accurately; in the following section we therefore focus on OTMP.

To reconstruct pre-eruptive volatile evolution in the OTMP, we applied the multistart MATLAB modelling approach of Lormand et al. (2024), which incorporates the temperature-dependent, non-ideal thermodynamic model for F, Cl, and OH in apatite of Li and Costa (2020), with an H_2O speciation model following Zhang (1999). In the model, volatile saturation occurs when the melt H_2O concentration reaches a pre-defined saturation level, and halogens are distributed between melt + crystals ± fluid using bulk crystal-melt and fluid-melt partition coefficients. The model setup is explained in detail by Lormand et al. (2024). The apatites with anomalously high halogen contents ($X_{Cl}/X_{OH} > 0.9$, $X_F/X_{OH} > 40$) were excluded, as the model does not account for late-stage processes. We first attempted to model the whole population as a single dataset with X_{Cl}/X_{OH} increasing as MgO decreases (Supplementary Fig. 1). This produced good fits to the data (Supplementary Fig. 2), with a fluid-undersaturated magma at 865 °C, but required unacceptably high bulk crystal-melt partition coefficients for H_2O $\left(D^{xl-m} \sim 1\right)$ which cannot be satisfied with the anhydrous mineral assemblage observed in the basalts.

We therefore tested a two-step model, which generated an excellent fit to the data (Table 1, Fig. 10). The first step simulates 80% H_2O-undersaturated fractional crystallization over a range of temperature (from 1070 °C to 880 °C, consistent with temperature constraints for basalts in the volcanic complex; Tadesse et al., 2023). Using the model to perform a sensitivity analysis on the input parameters (Supplementary Fig. 3–6), the best fitting runs suggests initial melt volatile concentrations of 0.7–1.5 wt% H_2O, 250–500 ppm Cl, and 150–300 ppm F. Bulk crystal-melt partition coefficients are 0.05–0.1 for Cl, 0.3–0.5 for F and 0.01–0.07 for H_2O, which seem reasonable for the observed mineral assemblage. The storage pressure for H_2O-undersaturated crystallization is constrained between the calculated final H_2O concentration, which is 4.5 ± 1.2 wt% H_2O for the 20 best-fitting runs, and the pre-defined H_2O saturation level of 6.1 ± 0.4 wt% H_2O. This translates to a storage pressure of 75–160 MPa using the H_2O solubility model of Romano et al. (2021). There is a strong co-variance between initial H_2O and F (±Cl) concentrations in the successful model outputs, which means the data can be fitted well using higher (or lower) initial H_2O concentrations as long as the initial F varies similarly.

The target curve for the second step uses the calculated volatile concentrations from the end of the first step as input parameters and models a further 50% fractional crystallization to match the full range of the observed apatite compositions. For many of the best-fitting runs, this stage is also initially H_2O-undersaturated, and reaches saturation through a further 5–28% crystallization, with a pre-defined H_2O saturation level of 5.7 ± 0.5 wt% H_2O. The best-fitting runs suggest initial melt volatile concentrations of 4–5.5 wt% H_2O, 1500–2200 ppm Cl and 550–650 ppm F. Modelled bulk crystal-melt partition coefficients are 0.06–0.17 for Cl, 0.48–0.83 for F and 0.07–0.26 for H_2O. Modelled fluid-melt partition coefficients are 2–10 for Cl and 1–3 for F.

These results are very consistent with petrologic interpretation of

Table 1
Summary of initial conditions for the two-step thermodynamic models used to model apatite composition in the OTMP (mean and standard deviation of top 20 best fitting results; see text for details).

		Step 1 (H_2O-undersaturated	Step 2 (initially close to H_2O saturation)
Initial melt concentrations (wt%)	Cl	0.04 ± 0.0086	0.18 ± 0.023
	F	0.022 ± 0.0063	0.06 ± 0.0035
	H_2O	1.0 ± 0.33	5.1 ± 0.42
Bulk crystal-melt partition coefficients	D^{xl-m}_{Cl}	0.081 ± 0.036	0.11 ± 0.033
	D^{xl-m}_{F}	0.39 ± 0.078	0.65 ± 0.097
	D^{xl-m}_{H2O}	0.073 ± 0.047	0.15 ± 0.058
Bulk fluid-melt partition coefficients	D^{fl-m}_{Cl}	5.5 ± 2.3	5.2 ± 2.6
	D^{fl-m}_{F}	1.8 ± 0.7	2.3 ± 0.64
H_2O sat		6.1 ± 0.4	5.7 ± 0.54
T° (°C)		1070–880	880–800
Degree of fractionation (%)		80	50

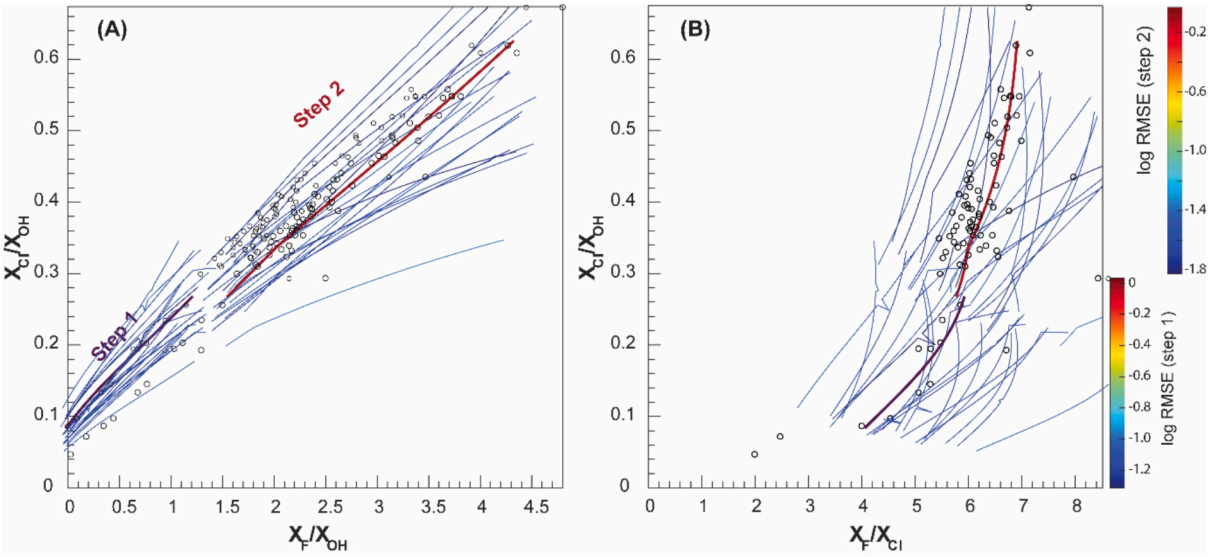

Fig. 10. Modelled volatile evolution trends OTMP apatites are indicated in the bivariate plots. The melt volatile composition are recovered in two steps. Step 1 is H_2O-undersaturated condition with parameters of bulk crystal-melt ($D_{Cl}^{xl-m} \sim 0.06$, $D_F^{xl-m} \sim 0.37$, and $D_{H2O}^{xl-m} \sim 0$) and fluid-melt partition coefficients ($D_{Cl}^{fl-m} \sim 20$ and $D_F^{fl-m} \sim 0.5$). Step 2 is initially close to H_2O saturation and is reproduced with bulk crystal-melt ($D_{Cl}^{xl-m} \sim 0.06, D_F^{xl-m} \sim 0.65$, and $D_{H2O}^{xl-m} \sim 0.15$) and fluid-melt partition coefficients ($D_{Cl}^{fl-m} \sim 3$ and $D_F^{fl-m} \sim 1.5$). The thermodynamic model of Lormand et al. (2024) is utilized for the modelling.

other magmatic systems in the MER. For example, fluid-melt partition coefficients are inferred to be 1.75 for F and 3 for Cl, based on melt inclusion data from Kone (Iddon and Edmonds, 2020). The same study used trace element compositions to infer 85% fractional crystallization from mafic parental melts to form trachyte (our step 1), followed by a further 40% fractionation to form pantellerite (our step 2). Maximum H_2O contents of olivine-hosted melt inclusions at Kone and Butajira contain 1–1.5 wt% H_2O, whereas quartz-hosted melt inclusions for Kone and Aluto contain up to 6.5 wt% H_2O (Iddon and Edmonds, 2020).

Our combined analysis of apatites and melt inclusions therefore offers a powerful forensic tool for reconstructing pre-eruptive volatile evolution. The modelling results support water saturation at the later stage of crystallization process. This interpretation is consistent with previous observations of unrest and degassing at these volcanoes (e.g., Hunt et al., 2017; Albino and Biggs, 2021), likely reflecting localised volatile saturation at the roof of a largely H_2O-undersaturated magma reservoir. Progressive crystallization concentrates dissolved H_2O in the melt, whereas volatile-poor magma recharge from depth could have temporarily suppressed volatile contents, maintaining undersaturated conditions within the reservoir (e.g., Ruprecht and Bachmann, 2010; Stock et al., 2016; Cassidy et al., 2016; Degruyter et al., 2017). Although there is no clear evidence for magma mixing at Tullu Moye and Boset-Bericha volcanic eruptions, we propose that progressive enrichment in dissolved H_2O eventually drove the system to saturation, triggering eruption in the absence of any external forcing.

5.3. *Pre-eruptive magma volatile content variability and volcanological implications*

Our models successfully reproduce the main compositional trends observed in apatite inclusions and microphenocrysts through protracted volatile-undersaturated, and then near saturated crystallization. This indicates that, during its evolutionary history, the main magma storage zone remained volatile-undersaturated for a while. A subset of apatite microphenocrysts from YTMP and Boset-Bericha unit #6 deviate from the main trend at moderate to low X_{Cl}/X_{OH}, likely reflecting crystallization in cooler parts of the reservoir prior to H_2O saturation. Following the interpretation of Stock et al. (2018), these crystals likely formed at depth, possibly near the reservoir margins, and were subsequently entrained into the eruptive magma. Minimum saturation pressures for the main magma body, obtained by converting H_2O solubility using the model of Romano et al. (2021) and independent MagmaSat calculations (Ghiorso and Gualda, 2015), reach up ~160 MPa (~6 km, assuming a crustal density of 2800 kg/m^3; Wilks et al., 2017), consistent with clinopyroxene barometry estimates (4 ± 11 km, Tadesse et al., 2023) and magnetotelluric observations (~4 km; Samrock et al., 2018; Samrock et al., 2021). As magmas ascend from these deeper reservoirs, they degas H_2O, resulting in low H_2O concentrations in matrix glass. However, similar Cl and F concentrations in melt inclusions and matrix glasses demonstrate that halogen degassing was limited, despite the high fluid-melt partition coefficient (e.g., $D_{Cl}^{fl-m} > 1$; Signorelli and Carroll, 2000). Relatively undepleted Cl contents in the glass are consistent with kinetic disequilibrium during rapid ascent, inhibiting Cl partitioning into the vapour phase (Webster et al., 1993; Barclay et al., 1996; Shea et al., 2014).

In contrast, apatite and melt inclusions from OTMP are compositionally distinct, showing markedly higher Cl and trace element contents (i.e., MgO) than those from the other eruptions. This likely reflects crystallization from a chemically different, more primitive melt. The direction of melt differentiation is preserved in the host mineral phases, which shield apatite and melt inclusions from re-equilibration. OTMP deposits also contain more primitive clinopyroxene phenocrysts (i.e., higher Mg#; Fig. 4); supporting the interpretation that OTMP magma was less evolved. Following this eruption, the Tullu Moye magma reservoir underwent further crystallization and differentiation, increasing volatile and trace element concentrations that ultimately fed the YTMP eruption. The clinopyroxene crystals from YTMP show reverse zoning with Al-Ti-Fe-rich cores (Tadesse et al., 2023). Thus, the low volatile concentration (i.e., Cl) in YTMP may be related to injection of fresh volatile-poor magma. At Boset-Bericha, although clinopyroxene chemistry records a slight temporal change in magma evolution, these differences were not sufficient to produce major compositional changes in volatiles or trace elements between eruptions.

Our dataset shows that peralkaline magma reservoirs can remain volatile-undersaturated for a significant time of their evolution. Although it remains difficult to pinpoint exactly how late this volatile-undersaturated state was reached, previous work on other peralkaline system suggests that such conditions could be sustained until days

before eruption (e.g., Stock et al., 2016; Stock et al., 2018). Many eruptions worldwide have occurred with minimal or no clear precursory unrest (e.g., Calbuco: Arzilli et al., 2019; Nyiragongo: Smittarello et al., 2022; Veniaminof: Li et al., 2025). While these systems differ in magma composition and tectonic setting from peralkaline rift volcanism, they nonetheless demonstrate that limited precursory signals can precede eruption across a broad range of volcanic contexts. This challenges traditional monitoring approaches, which often rely on seismicity and ground deformation. Although deformation pulses and/or seismicity have been observed in the MER, they do not always immediately precede eruption, but are usually interpreted to reflect shallow intrusions of magma, for example the emplacement of dikes (e.g., Temtime et al., 2020; Ayele et al., 2024; Keir et al., 2025; Lewi et al., 2025). Intermittent leakage of volatiles may provide early warning signals (e.g., de Moor et al., 2016; Paonita et al., 2021), emphasizing the need for high-temporal-resolution geochemical and isotopic monitoring of fumarolic gases in conjunction with geophysical data.

6. Conclusion

Apatite and melt inclusions together provide a robust means to constrain the pre-eruptive volatile content and behaviour of magmatic systems. In the peralkaline explosive eruptions of Tullu Moye and Boset-Baricha, apatite records prolonged volatile-undersaturated conditions during the crystallization of magma stored at shallow crustal levels (~4–6 km depth), consistent with present-day magma storage depths beneath silicic volcanoes in the MER and many silicic systems worldwide. Combined with thermodynamic modelling of volatile species, the new collected dataset suggest that magmatic differentiation was the primary control on volatile evolution. Apatite and melt inclusions from the OTMP are compositionally distinct, displaying higher Cl and trace element contents (i.e., MgO) compared to those from subsequent comenditic eruptions in Tullu Moye and Boset-Bericha volcanoes. This likely reflects crystallization from a more primitive melt, associated with early-stage clinopyroxene phenocrysts of OTMP. Following this phase, the Tullu Moye magma reservoir underwent further crystallization and fresh magma ejection, enriching the melt in volatiles and trace elements that ultimately supplied the YTMP eruption. In contrast, the Boset-Bericha deposits show no comparable variation in magma composition between the subsequent eruptions, suggesting no significant temporal advancement in magma evolution. While this study focuses on Tullu Moye and Boset-Bericha, our integrated approach can be broadly applied to reconstruct the temporal evolution of pre-eruptive volatile behaviour in other volcanic systems.

CRediT authorship contribution statement

Amdemichael Zafu Tadesse: Writing – review & editing, Writing – original draft, Visualization, Project administration, Methodology, Investigation, Funding acquisition, Formal analysis, Data curation, Conceptualization. **V.C. Smith:** Writing – review & editing, Supervision, Methodology, Data curation, Conceptualization. **K. Fontijn:** Writing – review & editing, Supervision, Investigation, Funding acquisition, Data curation, Conceptualization. **J.C.M. De Hoog:** Writing – review & editing, Methodology, Data curation. **D.J. Colby:** Writing – review & editing, Software, Methodology. **M.C.S. Humphreys:** Writing – review & editing, Software, Methodology, Conceptualization. **T.A. Mather:** Writing – review & editing, Supervision, Methodology, Funding acquisition, Conceptualization. **D.M. Pyle:** Writing – review & editing, Supervision, Methodology, Funding acquisition, Conceptualization.

Declaration of competing interest

The authors declare that they have no known competing financial interests or personal relationships that could have appeared to influence the work reported in this paper.

Acknowledgments

AT is supported by a Fondation Wiener-Anspach (FWA) postdoctoral fellowship. Laboratory analysis costs were covered by an FWA collaborative project awarded to KF, TM, and DP. A portion of the Secondary Ion Mass Spectrometry time was granted by NERC through the Ion Micro-Probe Facility in Edinburgh (grant IMF768/0424). AT is under Lamont-Doherty Earth Observatory postdoctoral fellowship grant during the submission of this manuscript. We also thank Krzysztof Sokół for assistance during analysis on the SEM instrument. MCSH and DJC received funding from the European Research Council (ERC) under the European Union's Horizon 2020 research and innovation programme (grant agreement No 864923). Our gratitude goes to Fabio Arzilli and one anonymous reviewer for detailed and constructive comments, which improved the paper. We thank Claudia Romano for the editorial handling.

Appendix A. Supplementary data

Supplementary data to this article can be found online at https://doi.org/10.1016/j.chemgeo.2026.123362.

Data availability

Data shared with supplementary file

References

Albino, F., Biggs, J., 2021. Magmatic processes in the East African Rift system: insights from a 2015–2020 Sentinel-1 InSAR survey. Geochem. Geophys. Geosyst. 22 (3), e2020GC009488.
Anenburg, M., Chen, J., Gardiner, M.G., de Hoog, J.C., Humphreys, M.C., Missen, O.P., Mills, S.J., Pašić, B., 2025. Silica substituted carbonate apatite: synthesis and analytical challenges. J. Mater. Chem. B 13 (32), 9968–9981.
Arzilli, F., Morgavi, D., Petrelli, M., Polacci, M., Burton, M., Di Genova, D., Spina, L., La Spina, G., Hartley, M.E., Romero, J.E., Fellowes, J., Diaz-Alvarado, J., Perugini, D., 2019. The unexpected explosive sub-Plinian eruption of Calbuco volcano (22–23 April 2015, southern Chile): triggering mechanism implications. J. Volcanol. Geotherm. Res. 378, 35–50.
Ayele, A., Luckett, R., Baptie, B., Whaler, K., 2024. The 2015 earthquake swarm in the Fentale volcanic complex (FVC): a geohazard risk for Ethiopia's commercial route to the Djibouti port. J. Afr. Earth Sci. 213, 105236.
Barclay, J., Carroll, M.R., Houghton, B.F., Wilson, C.J.N., 1996. Pre-eruptive volatile content and degassing history of an evolving peralkaline volcano. J. Volcanol. Geotherm. Res. 74 (1–2), 75–87.
Boccaletti, M., Mazzuoli, R., Bonini, M., Trua, T., Abebe, B., 1999. Plio-Quaternary volcanotectonic activity in the northern sector of the Main Ethiopian Rift: relationships with oblique rifting. J. Afr. Earth Sci. 29 (4), 679–698.
Bonini, M., Corti, G., Innocenti, F., Manetti, P., Mazzarini, F., Abebe, T., Pecskay, Z., 2005. Evolution of the Main Ethiopian Rift in the frame of Afar and Kenya rifts propagation. Tectonics 24 (1).
Boyce, J.W., Hervig, R.L., 2009. Apatite as a monitor of late-stage magmatic processes at Volcán Irazú, Costa Rica. Contrib. Mineral. Petrol. 157, 135–145.
Boyce, J.W., Tomlinson, S.M., McCubbin, F.M., Greenwood, J.P., Treiman, A.H., 2014. The lunar apatite paradox. Science 344 (6182), 400–402.
Brotzu, P., Morbidelli, L., EM, P., Traversa, G., 1980. Volcanological and magmatological evidence of the Boset Volcanic complex (Main Ethiopian Rift). Atti Convegni Lincei 47, 317–366.
Candela, P.A., 1986. Toward a thermodynamic model for the halogens in magmatic systems: an application to melt-vapor-apatite equilibria. Chem. Geol. 57 (3–4), 289–301.
Casey, M., Ebinger, C., Keir, D., Gloaguen, R., Mohamed, F., 2006. Strain accommodation in transitional rifts: extension by magma intrusion and faulting in Ethiopian Rift magmatic segments. Geol. Soc. London Spec. 259, 143–163.
Cashman, K.V., Sparks, R.S.J., 2013. How volcanoes work: a 25 year perspective. Bulletin 125 (5–6), 664–690.
Cassidy, M., Castro, J.M., Helo, C., Troll, V.R., Deegan, F.M., Muir, D., Neave, D.A., Mueller, S.P., 2016. Volatile dilution during magma injections and implications for volcano explosivity. Geology 44 (12), 1027–1030.
Cassidy, M., Manga, M., Cashman, K., Bachmann, O., 2018. Controls on explosive-effusive volcanic eruption styles. Nat. Commun. 9 (1), 2839.
Chelle-Michou, C., Chiaradia, M., 2017. Amphibole and apatite insights into the evolution and mass balance of Cl and S in magmas associated with porphyry copper deposits. Contrib. Mineral. Petrol. 172 (11), 105.
Chernet, T., Hart, W.K., Aronson, J.L., Walter, R.C., 1998. New age constraints on the timing of volcanism and tectonism in the northern Main Ethiopian Rift–southern Afar transition zone (Ethiopia). J. Volcanol. Geotherm. Res. 80 (3–4), 267–280.

Corti, G., 2009. Continental rift evolution: from rift initiation to incipient break-up in the Main Ethiopian Rift, East Africa. Earth Sci. Rev. 96 (1–2), 1–53.
Dallara, E., Fulignati, P., Costa, S., Gioncada, A., Langone, A., Pistolesi, M., 2023. Apatite chemistry in shoshonitic magmas: insights into the volatile evolution at La Fossa volcano (Vulcano Island, Aeolian Arc, Italy). Lithos 454, 107238.
Danyushevsky, L.V., McNeill, A.W., Sobolev, A.V., 2002. Experimental and petrological studies of melt inclusions in phenocrysts from mantle-derived magmas: an overview of techniques, advantages and complications. Chem. Geol. 183 (1–4), 5–24.
Degruyter, W., Huber, C., Bachmann, O., Cooper, K.M., Kent, A.J., 2017. Influence of exsolved volatiles on reheating silicic magmas by recharge and consequences for eruptive style at Volcán Quizapu (Chile). Geochem. Geophys. Geosyst. 18 (11), 4123–4135.
Di Paola, G.M., 1972. The Ethiopian Rift Valley (between 7 00′ and 8 40′ lat. North). Bull. Volcanol. 36, 517–560.
Douce, A.E.P., Roden, M.F., Chaumba, J., Fleisher, C., Yogodzinski, G., 2011. Compositional variability of terrestrial mantle apatites, thermodynamic modeling of apatite volatile contents, and the halogen and water budgets of planetary mantles. Chem. Geol. 288 (1–2), 14–31.
Ebinger, C.J., Casey, M., 2001. Continental breakup in magmatic provinces: an Ethiopian example. Geology 29 (6), 527–530.
Fontijn, K., McNamara, K., Tadesse, A.Z., Pyle, D.M., Dessalegn, F., Hutchison, W., Mather, T.A., Yirgu, G., 2018. Contrasting styles of post-caldera volcanism along the Main Ethiopian Rift: Implications for contemporary volcanic hazards. J. Volcanol. Geotherm. Res. 356, 90–113.
Gaetani, G.A., O'Leary, J.A., Shimizu, N., Bucholz, C.E., Newville, M., 2012. Rapid reequilibration of H2O and oxygen fugacity in olivine-hosted melt inclusions. Geology 40 (10), 915–918.
Ghiorso, M.S., Gualda, G.A., 2015. An H_2O–CO_2 mixed fluid saturation model compatible with rhyolite-MELTS. Contrib. Mineral. Petrol. 169, 1–30.
Giordano, D., Russell, J.K., Dingwell, D.B., 2008. Viscosity of magmatic liquids: a model. Earth Planet. Sci. Lett. 271 (1–4), 123–134.
Goldoff, B., Webster, J.D., Harlov, D.E., 2012. Characterization of fluor-chlorapatites by electron probe microanalysis with a focus on time-dependent intensity variation of halogens. Am. Mineral. 97 (7), 1103–1115.
Gouin, P., 1979. Earthquake history of Ethiopia and the Horn of Africa, p. 256.
Humphreys, M.C., Kearns, S.L., Blundy, J.D., 2006. SIMS investigation of electron-beam damage to hydrous, rhyolitic glasses: implications for melt inclusion analysis. Am. Mineral. 91 (4), 667–679.
Humphreys, M.C., Smith, V.C., Coumans, J.P., Riker, J.M., Stock, M.J., de Hoog, J.C.M., Brooker, R.A., 2021. Rapid pre-eruptive mush reorganisation and atmospheric volatile emissions from the 12.9 ka Laacher See eruption, determined using apatite. Earth Planet. Sci. Lett. 576, 117198.
Hunt, J.A., Zafu, A., Mather, T.A., Pyle, D.M., Barry, P.H., 2017. Spatially variable CO 2 degassing in the main Ethiopian Rift: implications for Magma storage, volatile transport, and Rift-related emissions. Geochem. Geophys. Geosyst. 18 (10), 3714–3737.
Iddon, F., Edmonds, M., 2020. Volatile-rich magmas distributed through the upper crust in the Main Ethiopian Rift. Geochem. Geophys. Geosyst. 21 (6), e2019GC008904.
Jarosewich, E., Nelen, J.A., Norberg, J.A., 1980. Reference samples for electron microprobe analysis. Geostand. Newslett. 4 (1), 43–47.
Jochum, K.P., Stoll, B., Herwig, K., Willbold, M., Hofmann, A.W., Amini, M., Aarburg, S., Abouchami, W., Hellebrand, E., Mocek, B., Raczek, I., Stracke, A., Alard, O., Bouman, C., Becker, S., Dücking, M., Brätz, H., Klemd, R., De Bruin, D., Canil, D., Cornell, D., De Hoog, C.J., Dalpé, C., Danyushevsky, L., Eisenhauer, A., Gao, Y., Snow, J.E., Groschopf, N., Günther, D., Latkoczy, C., MarGuillong, M., Hauri, E.H., Höfer, H.E., Lahaye, Y., Horz, K., Jacob, D.E., Simone A. Kasemann, S.A., Kent, A.J. R., Ludwig, T., Zack, T., Mason, P.R.D., Meixner, A., Rosner, M., Misawa, K., Nash, B. P., Pfänder, J., Premo, W.R., Sun, W.D., Tiepolo, M., Vannucci, R., Vennemann, T., Wayne, D., Woodhead, J.D., 2006. Mpi-ding reference glasses for in situ microanalysis: new reference values for element concentrations and isotope ratios. Geochem. Geophys. Geosyst. 7 (2).
Jorgenson, C., Higgins, O., Petrelli, M., Bégué, F., Caricchi, L., 2022. A machine learning-based approach to clinopyroxene thermobarometry: model optimization and distribution for use in Earth sciences. J. Geophys. Res. Solid Earth 127 (4), e2021JB022904.
Keir, D., La Rosa, A., Pagli, C., Wang, H., Ayele, A., Lewi, E., Monterroso, F., Raggiunti, M., 2025. The 2024 Fentale diking episode in a slow extending continental rift. Geophys. Res. Lett. 52 (5), e2024GL113214.
Kent, A.J., 2008. Melt inclusions in basaltic and related volcanic rocks. Rev. Mineral. Geochem. 69 (1), 273–331.
Ketcham, R.A., 2015. Calculation of stoichiometry from EMP data for apatite and other phases with mixing on monovalent anion sites. Am. Mineral. 100 (7), 1620–1623.
Lange, R.L., Carmichael, I.S., 1990. Thermodynamic properties of silicate liquids with emphasis on density, thermal expansion and compressibility. Rev. Mineral. Geochem. 24 (1), 25–64.
Le Bas, LeMaitre, R.W., Streckeisen, A., Zanettin, B., Subcommission, I.U.G.S., on the Systematics of Igneous Rocks, 1986. A Chemical classification of volcanic rocks based on the total alkali-silica diagram. J. Petrol. 27 (3), 745–750.
Lewi, E., Biggs, J., Ayele, A., Wright, T., Pagli, C., Keir, D., Ali, Y., Assefa, G., Wang, H., La Rosa, A., Way, L., Mengistu, F., Loughlin, S., Grandin, R., Temtime, T., Birhanu, Y., Freymueller, J., Zheng, W., 2025. Scientific response to the 2024–2025 dyke intrusions in the Fentale-Dofen Region, Ethiopia: geophysical monitoring, surface manifestations, and hazard mapping. Bull. Volcanol. 87 (8), 64.
Li, H., Hermann, J., 2015. Apatite as an indicator of fluid salinity: an experimental study of chlorine and fluorine partitioning in subducted sediments. Geochim. Cosmochim. Acta 166, 267–297.
Li, H., Hermann, J., 2017. Chlorine and fluorine partitioning between apatite and sediment melt at 2.5 GPa, 800 C: A new experimentally derived thermodynamic model. Am. Mineral. 102 (3), 580–594.
Li, W., Costa, F., 2020. A thermodynamic model for F-Cl-OH partitioning between silicate melts and apatite including non-ideal mixing with application to constraining melt volatile budgets. Geochim. Cosmochim. Acta 269, 203–222.
Li, W., Costa, F., Nagashima, K., 2021. Apatite crystals reveal melt volatile budgets and magma storage depths at Merapi volcano, Indonesia. J. Petrol. 62 (4), egaa100.
Li, Y., Gregg, P.M., Lu, Z., Wang, J., 2025. Stealthy magma system behavior at Veniaminof Volcano, Alaska. Front. Earth Sci. 13, 1535083.
Llovet, X., Proenza, J.A., Pujol-Solà, N., Farré-de-Pablo, J., Campeny, M., 2020. Correction of secondary fluorescence across phase boundaries in electron probe microanalysis of mineral inclusions. Microsc. Microanal. 26 (5), 895–905.
Lloyd, A.S., Plank, T., Ruprecht, P., Hauri, E.H., Rose, W., 2013. Volatile loss from melt inclusions in pyroclasts of differing sizes. Contrib. Mineral. Petrol. 165, 129–153.
Lormand, C., Humphreys, M.C., Colby, D.J., Coumans, J.P., Chelle-Michou, C., Li, W., 2024. Volatile budgets and evolution in porphyry-related magma systems, determined using apatite. Lithos 480, 107623.
Macdonald, R., 1974. Nomenclature and petrochemistry of the peralkaline oversaturated extrusive rocks. Bull. Volcanol. 38, 498–516.
Macdonald, R., Bagiński, B., Ronga, F., Dzierżanowski, P., Lustrino, M., Marzoli, A., Melluso, L., 2012. Evidence for extreme fractionation of peralkaline silicic magmas, the Boseti volcanic complex, Main Ethiopian Rift. Mineral. Petrol. 104, 163–175.
McCubbin, F.M., Vander Kaaden, K.E., Tartèse, R., Boyce, J.W., Mikhail, S., Whitson, E. S., Bell, A.S., Anand, M., Franchi, I.A., Wang, J., Hauri, E.H., 2015. Experimental investigation of F, Cl, and OH partitioning between apatite and Fe-rich basaltic melt at 1.0–1.2 GPa and 950–1000°C. Am. Mineral. 100 (8–9), 1790–1802.
de Moor, J.M., Aiuppa, A., Avard, G., Wehrmann, H., Dunbar, N., Muller, C., Tamburello, G., Liuzzo, G.M., Moretti, R., Conde, V., Galle, B., 2016. Turmoil at Turrialba Volcano (Costa Rica): degassing and eruptive processes inferred from high-frequency gas monitoring. J. Geophys. Res. Solid Earth 121 (8), 5761–5775.
Moore, L.R., Gazel, E., Tuohy, R., Lloyd, A.S., Esposito, R., Steele-MacInnis, M., Hauri, E. H., Wallace, P.J., Bodnar, R.J., 2015. Bubbles matter: an assessment of the contribution of vapor bubbles to melt inclusion volatile budgets. Am. Mineral. 100 (4), 806–823.
Morimoto, N., 1988. Nomenclature of pyroxenes. Mineral. Petrol. 39 (1), 55–76.
Paonita, A., Liuzzo, M., Salerno, G., Federico, C., Bonfanti, P., Caracausi, A., Giuffrida, G., La Spina, A., Caltabiano, T., Gurrieri, S., Giudice, G., 2021. Intense overpressurization at basaltic open-conduit volcanoes as inferred by geochemical signals: the case of the Mt. Etna December 2018 eruption. Sci. Adv. 7 (36), eabg6297.
Piccoli, P., Candela, P., 1994. Apatite in felsic rocks; a model for the estimation of initial halogen concentrations in the Bishop Tuff (Long Valley) and Tuolumne Intrusive Suite (Sierra Nevada Batholith) magmas. Am. J. Sci. 294 (1), 92–135.
Piccoli, P.M., Candela, P.A., 2002. Apatite in igneous systems. Rev. Mineral. Geochem. 48 (1), 255–292.
Portnyagin, M., Almeev, R., Matveev, S., Holtz, F., 2008. Experimental evidence for rapid water exchange between melt inclusions in olivine and host magma. Earth Planet. Sci. Lett. 272 (3–4), 541–552.
Preece, K., Gertisser, R., Barclay, J., Berlo, K., Herd, R.A., Edinburgh Ion Microprobe Facility, 2014. Pre-and syn-eruptive degassing and crystallisation processes of the 2010 and 2006 eruptions of Merapi volcano, Indonesia. Contrib. Mineral. Petrol. 168, 1–25.
Qin, Z., Lu, F., Anderson, A.T., 1992. Diffusive reequilibration of melt and fluid inclusions. Am. Mineral. 77 (5–6), 565–576.
Reubi, O., Blundy, J., Varley, N.R., 2013. Volatiles contents, degassing and crystallisation of intermediate magmas at Volcan de Colima, Mexico, inferred from melt inclusions. Contrib. Mineral. Petrol. 165, 1087–1106.
Riker, J., Humphreys, M.C., Brooker, R.A., De Hoog, J.C., EIMF, 2018. First measurements of OH-C exchange and temperature-dependent partitioning of OH and halogens in the system apatite–silicate melt. Am. Mineral. 103 (2), 260–270.
Romano, P., Di Carlo, I., Andújar, J., Rotolo, S.G., 2021. Water solubility in trachytic and pantelleritic melts: an experimental study. Comptes Rendus. Géosci. 353 (S2), 1–17.
Ronga, F., Lustrino, M., Marzoli, A., Melluso, L., 2010. Petrogenesis of a basalt-comendite-pantellerite rock suite: the Boseti Volcanic complex (Main Ethiopian Rift). Mineral. Petrol. 98 (1), 227–243.
Ruprecht, P., Bachmann, O., 2010. Pre-eruptive reheating during magma mixing at Quizapu volcano and the implications for the explosiveness of silicic arc volcanoes. Geology 38 (10), 919–922.
Samrock, F., Grayver, A.V., Eysteinsson, H., Saar, M.O., 2018. Magnetotelluric image of transcrustal magmatic system beneath the Tulu Moye geothermal prospect in the Ethiopian Rift. Geophys. Res. Lett. 45 (23), 12–847.
Samrock, F., Grayver, A.V., Bachmann, O., Karakas, Ö., Saar, M.O., 2021. Integrated magnetotelluric and petrological analysis of felsic magma reservoirs: Insights from Ethiopian rift volcanoes. Earth Planet. Sci. Lett. 559, 116765.
Shea, T., Hellebrand, E., Gurioli, L., Tuffen, H., 2014. Conduit-to localized-scale degassing during Plinian eruptions: Insights from major element and volatile (Cl and H2O) analyses within Vesuvius AD 79 pumice. J. Petrol. 55 (2), 315–344.
Shishkina, T.A., Botcharnikov, R.E., Holtz, F., Almeev, R.R., Portnyagin, M.V., 2010. Solubility of H_2O-and CO_2-bearing fluids in tholeiitic basalts at pressures up to 500 MPa. Chem. Geol. 277 (1–2), 115–125.
Siegburg, M., Gernon, T.M., Bull, J.M., Keir, D., Barfod, D.N., Taylor, R.N., Abebe, B., Ayele, A., 2018. Geological evolution of the Boset-Bericha volcanic complex, Main Ethiopian Rift: 40Ar/39Ar evidence for episodic Pleistocene to Holocene volcanism. J. Volcanol. Geotherm. Res. 351, 115–133.

Signorelli, S., Carroll, M.R., 2000. Solubility and fluid-melt partitioning of Cl in hydrous phonolitic melts. Geochim. Cosmochim. Acta 64 (16), 2851–2862.
Smittarello, D., Smets, B., Barrière, J., Michellier, C., Oth, A., Shrevè, T., Grandin, R., Theys, N., Brenot, H., Cayol, V., Allard, P., Caudron, C., Chevrel, O., Darchambeau, F., De Buyl, P., Delhaye, L., Derauw, D., Ganci, G., Geirsson, H., Kamte, K.E., Kambale, M.J., Kambale, N.J., Keserka, M.C., Kervyn, M., Kimanuka, R. C., Le Mèvel, H., Molendijk, S., Namur, O., Poppe, S., Schmid, M., Subira, J., Wauthier, C., Yalire, M., d'Oreye, N., Kervyn, F., Syavulisembo Muhindo, A., 2022. Precursor-free eruption triggered by edifice rupture at Nyiragongo volcano. Nature 609 (7925), 83–88.
Stock, M.J., Humphreys, M.C., Smith, V.C., Johnson, R.D., Pyle, D.M., EIMF, 2015. New constraints on electron-beam induced halogen migration in apatite. Am. Mineral. 100 (1), 281–293.
Stock, M.J., Humphreys, M.C., Smith, V.C., Isaia, R., Pyle, D.M., 2016. Late-stage volatile saturation as a potential trigger for explosive volcanic eruptions. Nat. Geosci. 9 (3), 249–254.
Stock, M.J., Humphreys, M.C., Smith, V.C., Isaia, R., Brooker, R.A., Pyle, D.M., 2018. Tracking volatile behaviour in sub-volcanic plumbing systems using apatite and glass: Insights into pre-eruptive processes at Campi Flegrei, Italy. J. Petrol. 59 (12), 2463–2492.
Stormer, J.C., Pierson, M.L., 1993. Variation of F and Cl X-ray intensity due to anisotropic diffusion and electron microprobe analysis of apatite: an addendum. In: American Mineralogist Supplemental Data. http://www.minsocam.org/msa/amm in/supplemental_data/Stormer.html.
Tadesse, A.Z., Fontijn, K., Melaku, A.A., Gebru, E.F., Smith, V.C., Tomlinson, E., Barfod, D., Gopon, P., Bégué, F., Caricchi, L., Laha, P., Terryn, H., Gudbrandsson, S., Yirgu, G., Ayalew, D., 2022. Eruption frequency and magnitude in a geothermally active continental rift: the Bora-Baricha-Tullu Moye volcanic complex, Main Ethiopian Rift. J. Volcanol. Geotherm. Res. 423, 107471.
Tadesse, A.Z., Fontijn, K., Caricchi, L., Begue, F., Gudbrandsson, S., Smith, V.C., Gopon, P., Debaille, V., Laha, P., Terryn, H., Yirgu, G., Ayalew, D., 2023. Pre-eruptive storage conditions and magmatic evolution of the Bora-Baricha-Tullu Moye volcanic system, Main Ethiopian Rift. Lithos 442, 107088.
Temtime, T., Biggs, J., Lewi, E., Ayele, A., 2020. Evidence for active rhyolitic dike intrusion in the northern Main Ethiopian Rift from the 2015 Fentale seismic swarm. Geochem. Geophys. Geosyst. 21 (6), e2019GC008550.
Weber, G., Blundy, J., 2024. A machine learning-based thermobarometer for magmatic liquids. J. Petrol. 65 (4), egae020.
Webster, J.D., Piccoli, P.M., 2015. Magmatic apatite: a powerful, yet deceptive, mineral. Elements 11 (3), 177–182.
Webster, J.D., Taylor, R.P., Bean, C., 1993. Pre-eruptive melt composition and constraints on degassing of a water-rich pantellerite magma, Fantale volcano, Ethiopia. Contrib. Mineral. Petrol. 114, 53–62.
Webster, J.D., Tappen, C.M., Mandeville, C.W., 2009. Partitioning behavior of chlorine and fluorine in the system apatite–melt–fluid. II: felsic silicate systems at 200 MPa. Geochim. Cosmochim. Acta 73 (3), 559–581.
Wilks, M., Kendall, J.M., Nowacki, A., Biggs, J., Wookey, J., Birhanu, Y., Ayele, A., Bedada, T., 2017. Seismicity associated with magmatism, faulting and hydrothermal circulation at Aluto Volcano, Main Ethiopian Rift. J. Volcanol, Geoth. Res. 340, 52–67.
Wolfenden, E., Ebinger, C., Yirgu, G., Deino, A., Ayalew, D., 2004. Evolution of the northern Main Ethiopian rift: birth of a triple junction. Earth Planet. Sci. Lett. 224 (1–2), 213–228.
Wong, K., Ferguson, D., Wieser, P., Morgan, D., Edmonds, M., Tadesse, A.Z., Yirgu, G., Harvey, J., Hammond, S., 2023. Focused mid-crustal magma intrusion during continental break-up in Ethiopia. Geophys. Res. Lett. 50 (11), e2023GL103257.
Zhang, Y., 1999. H_2O in rhyolitic glasses and melts: measurement, speciation, solubility, and diffusion. Rev. Geophys. 37 (4), 439–516.
Zimmer, M.M., Plank, T., Hauri, E.H., Yogodzinski, G.M., Stelling, P., Larsen, J., Singer, B., Jicha, B., Mandeville, C., Nye, C.J., 2010. The role of water in generating the calc-alkaline trend: new volatile data for Aleutian magmas and a new tholeiitic index. J. Petrol. 51 (12), 2411–2444.